Article

Three-Dimensional Morphological Study of MnTe-like Structures by Assessment of Tortuosity Tensor Using Computational Fluid Dynamics

Giuseppe Prenesti [1,2] , Edoardo Walter Petrassi [1], Caterina Guzzo [1], Silvia Mannella [1], Francesco Stellato [1], Laura Crisafulli [1], Giulia Azzato [1,†] , Andrea Katovic [1], Agostino Lauria [3] and Alessio Caravella [1,2,*]

1 Department of Computer Engineering, Modelling, Electronics and Systems Engineering (DIMES), University of Calabria, via P. Bucci, Cubo 42C, 87036 Rende, Italy; giuseppe.prenesti@unical.it (G.P.); edoriguard@gmail.com (E.W.P.); cguzzo5@gmail.com (C.G.); silviamannella726@gmail.com (S.M.); stlfnc01e18d086q@studenti.unical.it (F.S.); lauracri11@outlook.it (L.C.); giuliaazzato@gmail.com (G.A.); andrea.katovic@unical.it (A.K.)
2 Institute on Membrane Technology—National Research Council (CNR-ITM), via P. Bucci, Cubo 17C, 87036 Rende, Italy
3 Department of Engineering for Innovation, University of Salento (UNISALENTO), Corpo Z, Campus Ecotekne, SP.6 per Monteroni, 73047 Lecce, Italy; agostino.lauria@unisalento.it
* Correspondence: alessio.caravella@unical.it; Tel.: +39-0984-49-6051
† Current address: TECHFEM S.p.A.—Human and Sustainable Engineering, via Toniolo, 1/D, 61032 Fano, Italy.

Abstract: This paper focuses on a morphological study of the MnTe-like structures, carried out by the evaluation of the tortuosity tensor and other related parameters using a computational fluid dynamics approach recently developed by our research group. The present work focuses on all possible crystals—existing or not developed yet—having the same structure as that of the manganese telluride. This analysis provides new information not present yet in the open literature. The motivation behind this study lies in the importance of this type of structure in physics and material science. In particular, the structures investigated are anisotropic and bi-disperse, with two independent geometrical parameters controlling the structure shape: the ratio of the particle diameters (r_1) and the normalised inter-particle distance (r_2). Exploiting this fact, several different structures of the same family are created, changing these two parameters independently, also allowing inter-penetration of particles to enlarge the study's applicability. The results are primarily obtained in terms of the tortuosity tensor, needed to catch and quantify the anisotropy of the structures. Then, other morphological parameters, such as connectivity, principal diffusion directions, and anisotropy factors, are evaluated, obtaining in this way a novel morphological characterisation of the structure. It is found that high values of tortuosity are observed at lower and higher values of $\{r_1, r_2\}$, which means that there exists a minimum value between them. Additionally, the anisotropy factor is found to be higher at lower values of $\{r_1, r_2\}$ and lower at higher ones. This is in accordance with the fact that, as the inter-particle distance and the ratio between particle diameters increase, the structure enlarges, which implies a lower influence of the particle distribution and, thus, a gradually more isotropic structure.

Keywords: effective diffusivity; tortuosity tensor; anisotropy; connectivity; morphology

1. Introduction

The manganese telluride, MnTe, is a material of interest for a number of applications in physics and material science. In the relatively new branch of physics, called *spintronics*, which studies the intrinsic property of electrons called *spin* to be applied to storage, transfer, and manipulation of information pieces, MnTe is recognised as a promising material for exhibiting interesting magnetic and electronic properties.

Actually, this material has been studied at least since the sixties of last century. In particular, Kunitomi et al. (1964) [1] carried out a neutron diffraction study on MnTe, establishing that the manganese ion in MnTe has five unpaired electrons. Later, Allet et al. (1977) [2] evaluated the optical properties and electronic structure of MnTe, observing that it showed a relatively large energetic *p-d* overlap, which is typical in NiAs-structured materials. Wei et al. (1986) [3] modelled the structural, magnetic, and electronic properties of a zinc-blended-like MnTe structure, reporting peculiar properties related to ferromagnetic and antiferromagnetic spin ordering.

Oleszkiewicz et al. (1988) [4] analysed the optical and dielectric properties of MnTe thin films, estimating a direct energy gap of around 1.27 eV at room temperature. In order to improve the optical and magnetic properties, Wang et al. (1996) [5] synthesised novel ternary MnTe-based structures described by the general brute formula of $M_xMn_yTe_z$ (with M = Li or Na), studying the number of different phases and crystallographic structures generated from the addition of the Na element. Since these preliminary studies, the MnTe structures have shown several interesting magnetic properties, as reported by Kriegner et al. (2016) [6], who observed multiply stable anisotropic magneto-resistance memory in antiferromagnetic MnTe.

Han et al. (2018) [7] reported interesting semiconductor properties of zinc-stabilised manganese telluride for application in optoelectronics. Specifically, they observed a great reduction (from 100 up to 10,000 times lower) in the electrical conductivity of the wurzite MnTe with respect to the nickeline one when the zinc content is below 8 at%, explaining such an observation by the strong preference of the Zn atoms to rearrange in tetrahedral coordination more than in octahedral.

Luo et al. (2023) [8] fabricated polycrystalline $MnSb_2Te_4$ to reduce the thermal conductivity of the MnTe structure. They also showed that a further substitution of some Mn atoms with Ge ones further decreased the thermal conductivity, making these materials particularly promising for the fabrication of thermoelectric generators.

Li et al. (2023) [9] determined several thermodynamic and electronic parameters of Mn- and Mg-doped SnTe alloys, such as formation energies of defects, the nature of chemical bonding, and electronic structures, via a first-principles approach. They calculated that the solubility of Mg in the SnTe alloys is higher than that of Mn, with a more significant lattice distortion due to the Mn replacement in the Sn sites.

Recently, Shah et al. (2024) [10] developed a facile fabrication of a MnTe and graphene oxide (GO) nanostructure for applications to energy storage. In particular, such a nanocomposite structure shows an improved specific capacity and a significant retention rate of 99% over 2000 cycles, which is explained by considering the effective inter-penetration of MnTe into GO, causing an enhanced electron transfer rate as well as a larger electrochemical active area.

In the same field, Selestina et al. (2024) [11] investigated MnTe as a potential p-type semiconductor thermoelectric material to be used in the middle-temperature range, incorporating magnesium in the structure. In particular, they observed a synergistic effect of magnesium, which increases the electrical property and reduced the thermal conductivity.

Autieri (2024) [12] underlined that it is predicted that a newly observed kind of magnetism, known as alter-magnetism, can arise in some class materials, with such a property being more useful than ferromagnetism for some applications. At the same time, Lee et al. (2024) [13] reported direct spectroscopic evidence for alter-magnetism in α-MnTe, which represents another significant peculiarity of this type of structure.

The number of possible applications even increases if considering that Chowde Gowda et al. (2024) [14] synthesised MnTe quantum dots (QDs) for exploitation in photocatalysis. In particular, they showed that the quantum confinement leadsleads to a larger energy bandgap, which in turn leads to a good photocatalytic degradation efficiency boosted by the enhanced magnetic field.

Despite the number of aforementioned studies, there are no examples of applications based on morphological properties, mainly because there is a lack of information for

this type of structure. One important application that deserves to be explored for MnTe-like structures is the gas separation, including the material, for example, as a layer of multifunctional composite membranes (see, for example, references [15–17]), for which the evaluation of the effective diffusivity tensor and, thus, of the tortuosity tensor, is crucial [18].

All these studies highlight that no analyses have been performed yet on the morphological properties of this type of structure, which, in our opinion, is a gap to be filled to possibly apply existing and new materials to gas separation and mass-transfer-based technology. In fact, to the best of our knowledge, there is no morphological study in the literature reporting the assessment of the tortuosity tensor of MnTe-like structures.

In this context, the aim of this work is to report new morphological properties of MnTe-like structures that have not been reported yet in the open literature. The importance of such morphology data lies in the possibility of developing new applications based on mass transfer selectivity, such as gas separation by multilayer membranes.

Specifically, here, we evaluate the diffusional effective diffusivity tensor and, from it, the diffusional tortuosity tensor, for different MnTe-like structures created in the CAD environment of the commercial software Comsol Multiphysics® by changing its structural parameters.

For this purpose, we use the novel methodology based on a computational fluid dynamics (CFD) approach recently developed by our research group [19] to evaluate the morphological properties of complex porous structures. The related CFD simulations are performed in the same software. The details of our investigation are reported in the next sections.

2. Methodology

Figure 1 summarises the main steps for the evaluation of the morphological parameters of the structure considered in this work. The following sections report the details of the construction of the geometries considered for simulations as well as the meshing and simulation settings.

Methodology Flow Diagram
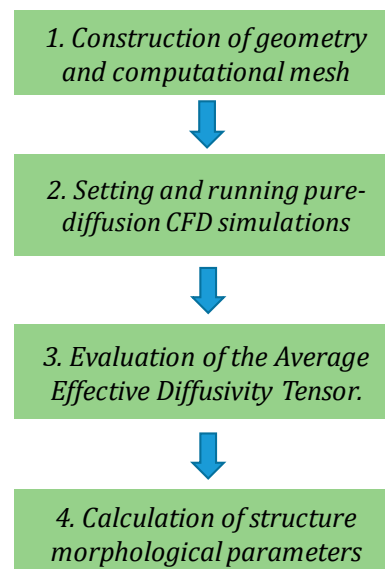

Figure 1. Flow diagram of the methodology.

2.1. Geometry

The original manganese telluride (MnTe) has a hexagonal crystal structure that is determined by two main parameters: the MnTe bond length, *d* (equal to 2.68 Å [20]), and the height of the unit cell, *c* (equal to 5.946 Å [9]). The edge of the base of the unit

cell, a, is calculated by using these two parameters according to the following equation (Equation (1) [9]):

$$a = \sqrt{3\left(d^2 + \frac{c^2}{16}\right)} \tag{1}$$

Figure 2 shows an example of the unit cell considered for simulation, where symmetry is exploited. In this scheme, the three orthographic views are shown along with the parameters a and c characterising the unit cell of the MnTe structure.
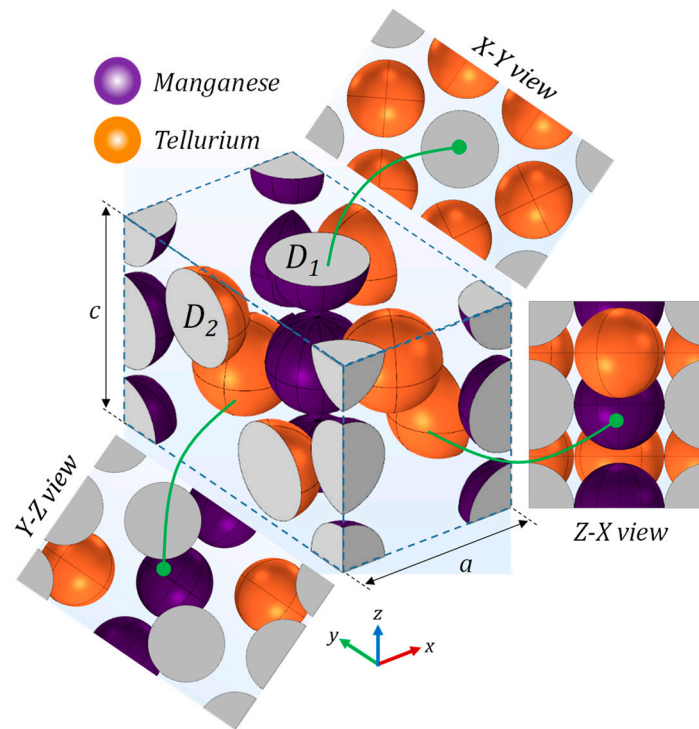
Figure 2. Example of the unit cell considered for simulation. The lengths D_1 and D_2 are the diameters of the particle 1 (manganese) and particle 2 (tellurium).

Since this structure is characterised by two different particles with independent size (bi-disperse structure), given the same type of unit cell, the original ratio, $r_0 \equiv a/c$, which is kept constant in the present work, is 0.87451 from Equation (1). Therefore, once r_0 is fixed, the family of the MnTe-like structures can be constructed by changing three different geometrical quantities, which in the present study are chosen to be: the diameter (D_1) of the particle 1 (nominally manganese), the diameter (D_2) of the particle 2 (nominally tellurium), and the edge of the base of the unit cell (a).

However, tortuosity—as well as all the morphological parameters of a structure, such as porosity, anisotropy, and diffusional preferential paths—does not depend on the particular scale of investigation and, thus, the aforementioned three independent geometrical parameters—D_1, D_2, and a—can be normalised with respect to one of them.

This implies that the structure properties are controlled by two dimensionless parameters only. In the present paper, we chose D_1 as such a reference geometrical length for normalisation purpose, which means that the controlling parameters are specified as follows (Equation (2)):

$$r_o \equiv \frac{a}{c} \text{ (fixed)}, \ r_1 \equiv \frac{a}{D_1}, \ r_2 \equiv \frac{D_2}{D_1} \tag{2}$$

Equation (3) shows the other structure parameters obtained from the controlling ones. Furthermore, to enlarge the applicability of the present study, we also allowed inter-penetration of the particles:

$$\frac{c}{D_1} = \frac{1}{r_o} \frac{a}{D_1} = \frac{r_1}{r_o}$$
$$\frac{d}{D_1} = \sqrt{\frac{1}{3}r_1^2 - \frac{1}{16}\left(\frac{c}{D_1}\right)^2} = r_1\sqrt{\frac{1}{3} - \frac{1}{16r_o}}$$

(3)

The ranges of the values for r_1 and r_2 used in the simulation are reported in Table 1. It is noted that, for simulation purposes, we need to obtain the negative void space of the structures, which is the domain available to diffusion (Figure 3).

Table 1. Values for r_1 and r_2 parameters.

Parameters	Pairs of Values
$\{r_1, r_2\}$	{1.4, 1}, {1.5, 1}, {1.6, 1}, {1.94, 1}, {1, 0.01}, {3, 3}, {5, 5}, {8, 8}, {9, 10}
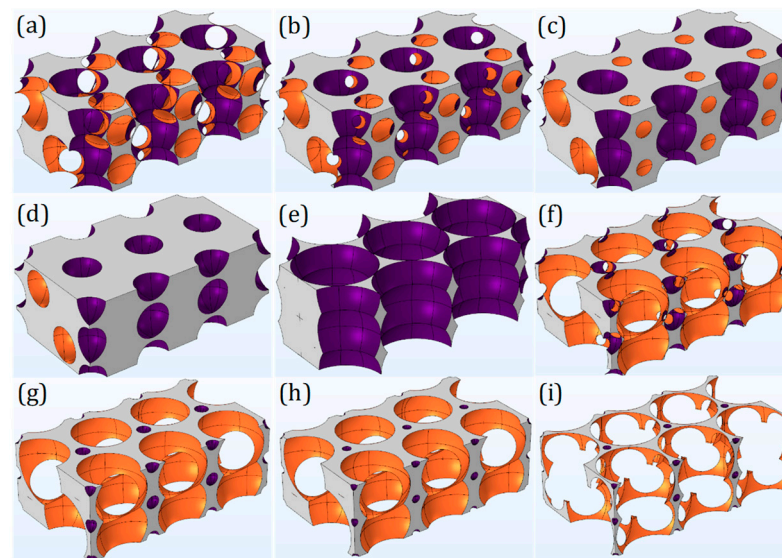
Figure 3. All the structures considered for simulation: (**a**) $r_1 = 1.4$, $r_2 = 1$; (**b**) $r_1 = 1.5$, $r_2 = 1$; (**c**) $r_1 = 1.6$, $r_2 = 1$; (**d**) $r_1 = 1.94$, $r_2 = 1$; (**e**) $r_1 = 1$, $r_2 = 0.01$; (**f**) $r_1 = 3$, $r_2 = 3$; (**g**) $r_1 = 5$, $r_2 = 5$; (**h**) $r_1 = 8$, $r_2 = 8$; (**i**) $r_1 = 9$, $r_2 = 10$.

2.2. Simulation Settings

Once we constructed the geometries, the appropriate physics has to be applied to them. In order to better understand the calculation approach used in the present work, the details of our previous work are briefly summarised in this section.

As mentioned above, to evaluate the tortuosity tensor along with the derived morphological parameters, we use a novel approach recently developed by our research group, consisting of carrying out simulations in pure-diffusion conditions along three different directions—namely, x, y, and z—corresponding to the main directions of a parallelepiped unit cell [19].

The details of our novel methodology, its novelties, and validation are already reported extensively in [19], where the approach is validated in terms of tortuosity values of several FCC structures obtained by a different numerical methodology, i.e., by the random-walk algorithm [21].

The characterisation of the structure anisotropy is performed by the so-called *average effective diffusivity tensor* (Equation (4)), which is defined analogously to the local binary

diffusivity tensor appearing in the constitutive equations of the pure-diffusive flux of a species in a 3D space [19]:

$$\begin{bmatrix} \bar{J}_{T,x} \\ \bar{J}_{T,y} \\ \bar{J}_{T,z} \end{bmatrix} = - \begin{bmatrix} \overline{D}_{e,xx} & \overline{D}_{e,xy} & \overline{D}_{e,xz} \\ \overline{D}_{e,yx} & \overline{D}_{e,yy} & \overline{D}_{e,yz} \\ \overline{D}_{e,zx} & \overline{D}_{e,zy} & \overline{D}_{e,zz} \end{bmatrix} \cdot \begin{bmatrix} \frac{\Delta C}{\Delta x} \\ \frac{\Delta C}{\Delta y} \\ \frac{\Delta C}{\Delta z} \end{bmatrix} \qquad \Leftrightarrow \quad \bar{J}_T = -\underline{\underline{D}}_e \cdot \Delta C \qquad (4)$$

The advantage of the used approach lies in the simplicity of the simulations that have to be carried out to obtain the desired morphological properties, as pure-diffusion simulations are suitable to be run even by non-experts in numerical calculation.

According to this approach, the form reported in Equation (4) is inverted in order to express the components of the gradient as functions of the components of the corresponding flux (Equation (5)), where the coefficients $\overline{R}_{e,ij}$ in Equation (5) are *diffusion resistivities* [19]:

$$\begin{cases} \frac{\Delta C}{\Delta x} = -\overline{R}_{e,xx}\bar{J}_{T,x} - \overline{R}_{e,xy}\bar{J}_{T,y} - \overline{R}_{e,xz}\bar{J}_{T,z} \\ \frac{\Delta C}{\Delta y} = -\overline{R}_{e,yx}\bar{J}_{T,x} - \overline{R}_{e,yy}\bar{J}_{T,y} - \overline{R}_{e,yz}\bar{J}_{T,z} \\ \frac{\Delta C}{\Delta z} = -\overline{R}_{e,zx}\bar{J}_{T,x} - \overline{R}_{e,zy}\bar{J}_{T,y} - \overline{R}_{e,zz}\bar{J}_{T,z} \end{cases} \qquad (5)$$

The form in Equation (5) allows us to calculate the resistivity coefficients along a specific direction, as it is only necessary to carry out simulations in which the other two average fluxes, $J_{T,i}$, different from that in the considered specific direction, are zero.

Equation (6) shows an example of the calculation for the x components of the resistivity tensor, for which the fluxes along the y and z directions ($J_{T,y}$ and $J_{T,z}$) are set to zero by choosing the boundary conditions reported in Figure 4 [19]:

$$\begin{cases} \frac{\Delta C}{\Delta x}\Big|_{\bar{J}_{T,y}=\bar{J}_{T,z}=0} = -\overline{R}_{e,xx}\bar{J}_{T,x} \\ \frac{\Delta C}{\Delta y}\Big|_{\bar{J}_{T,y}=\bar{J}_{T,z}=0} = -\overline{R}_{e,yx}\bar{J}_{T,x} \\ \frac{\Delta C}{\Delta z}\Big|_{\bar{J}_{T,y}=\bar{J}_{T,z}=0} = -\overline{R}_{e,zx}\bar{J}_{T,x} \end{cases} \Rightarrow \begin{cases} \overline{R}_{e,xx} = -\dfrac{\frac{\Delta C}{\Delta x}\big|_{\bar{J}_{T,y}=\bar{J}_{T,z}=0}}{\bar{J}_{T,x}} \\ \overline{R}_{e,yx} = -\dfrac{\frac{\Delta C}{\Delta y}\big|_{\bar{J}_{T,y}=\bar{J}_{T,z}=0}}{\bar{J}_{T,x}} \\ \overline{R}_{e,zx} = -\dfrac{\frac{\Delta C}{\Delta z}\big|_{\bar{J}_{T,y}=\bar{J}_{T,z}=0}}{\bar{J}_{T,x}} \end{cases} \qquad (6)$$

Therefore, each simulation allows the evaluation of three components of the resistivity tensor, which means that three different simulations are needed for each geometry to evaluate the entire tensor.

It is specified here that other types of boundary conditions are not suitable to evaluate the tortuosity tensor, as for this purpose it is necessary both to set a concentration difference along the investigated direction and, at the same time, to ensure that the flux streamlines enter the high-concentration surface and exit the low-concentration one (see Equations (5) and (6) for the mathematical details). These boundary conditions allowing tortuosity evaluation do not have to be confused with boundary conditions related to real applications, which need to be chosen according to the specific external conditions of the system investigated.
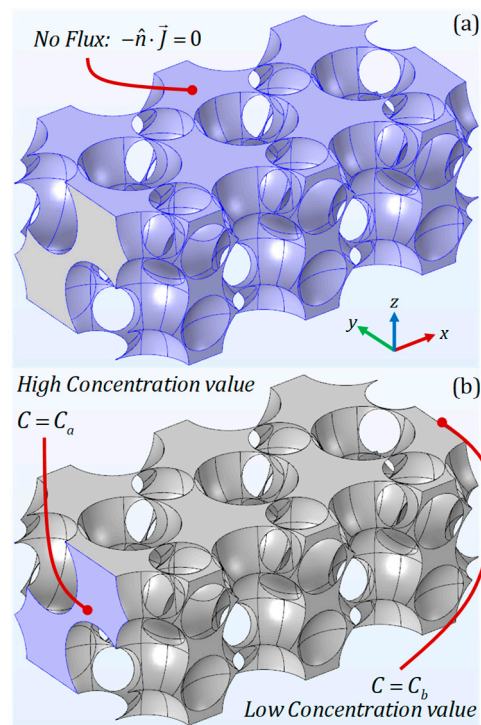
Figure 4. Computational domain, along with the corresponding boundary conditions—(**a**) zero flux, and (**b**) concentration set at the in-front boundaries—for a certain inter-penetrating particle structure corresponding to $r_1 = 1.4$, $r_2 = 0\ 1$. Example of *x*-direction.

Once the resistivity tensor is obtained, the effective diffusivity one is calculated by a simple inversion of it (Equation (7)):

$$\overline{\overline{D_e}} = \overline{\overline{R_e}}^{-1} \tag{7}$$

Afterwards, the diagonal form of the diffusivity tensor is evaluated, allowing us to identify the principal diffusional path represented by the eigenvectors. Finally, from the diagonal diffusivity tensor, we obtain the diagonal tortuosity tensor as the natural extension to the three-dimensional case (Equations (8) and (9)):

$$\underline{\underline{\tau}}^{(d)} = D\varepsilon \overline{\overline{D}}_e^{(d)-1} \tag{8}$$

$$\underline{\underline{\tau}}^{(d)} = \begin{bmatrix} \tau_{11}^{(d)} & & \\ & \tau_{22}^{(d)} & \\ & & \tau_{33}^{(d)} \end{bmatrix} \tag{9}$$
$$\left\{ \begin{array}{l} \text{Diagonal form of} \\ \text{Tortuosity Tensor} \end{array} \right\}$$

The overall tortuosity, τ_{ov}, is also evaluated, defined as the norm of the diagonal tortuosity tensor (Equation (10)):

$$\tau_{ov} \equiv \sqrt{\tau_{11}^{(d)^2} + \tau_{22}^{(d)^2} + \tau_{33}^{(d)^2}} \tag{10}$$

As important derived morphological parameters, we also evaluate the overall connectivity factor, φ_{ov} (Equation (11)), and the anisotropy factor, α (Equation (12)) [22] of the structure, the former of which is defined as the norm of the connectivity tensor, which

is in turn defined as the inverse of the tortuosity tensor, according to the works reported in [19,23,24].

The anisotropy factor is equivalently evaluated here using the principal connectivity factors reported in Equation (11) instead of using the eigenvalues of the effective diffusivity tensor, as originally carried out by Basser and Pierpaoli (1996) [22]:

$$
\underline{\underline{\varphi}}^{(d)} \equiv \underline{\underline{\tau}}^{(d)\,-1}
$$

$$
\begin{bmatrix} \varphi_{11}^{(d)} & & \\ & \varphi_{22}^{(d)} & \\ & & \varphi_{33}^{(d)} \end{bmatrix} \equiv \begin{bmatrix} \tau_{11}^{(d)} & & \\ & \tau_{22}^{(d)} & \\ & & \tau_{33}^{(d)} \end{bmatrix}^{-1} \tag{11}
$$

$$
\left\{ \text{Connectivity Tensor} \right\} \qquad \left\{ \text{Tortuosity Tensor} \right\}^{-1}
$$

$$
\varphi_{ov} \equiv \sqrt{\varphi_{11}^{(d)\,2} + \varphi_{22}^{(d)\,2} + \varphi_{33}^{(d)\,2}}
$$

$$
\alpha \equiv \frac{1}{\sqrt{6}} \frac{\sqrt{\left(\varphi_{11}^{(d)} - \overline{\varphi}\right)^2 + \left(\varphi_{22}^{(d)} - \overline{\varphi}\right)^2 + \left(\varphi_{33}^{(d)} - \overline{\varphi}\right)^2}}{\overline{\varphi}} \tag{12}
$$

$$
\overline{\varphi} = \frac{\varphi_{11}^{(d)} + \varphi_{22}^{(d)} + \varphi_{33}^{(d)}}{3}
$$

As an important remark, we underline that the diffusional tortuosity is a geometrical parameter independent of the particular species used for simulation [25,26], different from other types of tortuosity, such as thermal, acoustic, or hydraulic tortuosity, which depend on the particular field applied to generate the flux of a certain physical quantity [27–37]. In the present paper, we use the binary decane–oxygen mixture in all simulations, whose parameters are reported in Table 2.

Table 2. Operating conditions considered for simulation.

Parameter	Value
Binary mixture in pure diffusion (zero convection)	$\{C_{10}H_{22}, O_2\}$
Pressure, Pa	101,325
Mass fraction of species 1 (decane) over the higher-concentration area	$2 \cdot 10^{-4}$
Mass fraction of species 1 (decane) over the lower-concentration area	10^{-4}
Temperature, °C	25
Binary diffusivity, $m^2\,s^{-1}$	10^{-5}

2.3. Computational Mesh

Once having set up the simulation physics, the computational mesh of the structures needs to be built. As inter-penetration of particles is allowed in the present work, there can be part of the structure where the channel for diffusion is severely narrow, which implies high-concentration gradients. Therefore, the meshing procedure must be setup to account for such a situation, which can affect the simulation correctness. At the same time, the final results must be mesh independent.

In general, efficient meshing should be such that the elements are preferentially oriented along the flux direction, which, however, is not known before running the simulation. As the generated structures can be quite complex and, thus, the void channel can be oriented along different directions, a good strategy is to increase the mesh density in the narrowest channel. In our case, we find that our adaptive meshing procedure ensures an accuracy up to the fourth digit without prohibitively increasing the computational duty, which is satisfactory for our purpose. Other meshing strategies are also possible, such as the generation of a boundary layer near the surface. However, such a strategy is required

in CFD studies in the presence of convection and local eddy vortices in the bulk, which is not related to our pure-diffusion systems. In the present work, all meshes are built to ensure at least five elements (tetrahedral) in the narrowest channels of the structure, which ensured a semi-automatic meshing procedure.

To check the required mesh independency, we repeated all simulations by building two different computational meshes and ensuring three and five elements in the narrowest regions, respectively. By doing so, we found a difference in tortuosity values at the fourth decimal digit between the two cases (see Table 3).

Table 3. Mesh independency of the results for all the cases considered in this work.

| Tortuosity Components					
τ_{11}, $-$		τ_{22}, $-$		τ_{33}, $-$	
Number of Mesh Elements in the Narrowest Region					
3	5	3	5	3	5
5.53193	5.53181	5.23663	5.23651	1.44556	1.44544
7.45090	7.45078	2.86816	2.86804	2.05677	2.05665
2.11487	2.11475	1.59753	1.59741	1.17920	1.17908
1.18865	1.18853	1.18155	1.18143	1.10124	1.10112
2.03772	2.03760	2.03342	2.03330	1.30116	1.30104
3.50189	3.50177	2.78992	2.78980	2.56907	2.56895
2.66186	2.66174	2.56521	2.56509	1.72301	1.72289
2.68382	2.68370	2.61089	2.61077	1.71169	1.71157
8.15568	8.15572	6.44101	6.44117	6.31910	6.31909

Therefore, based on these preliminary results, we decided to use five elements for a matter of accuracy. Figure 5 shows an example of meshing for a certain structure with inter-penetrating particles, where a zoomed detail is reported to highlight the shape of the computational mesh in the narrowest regions.
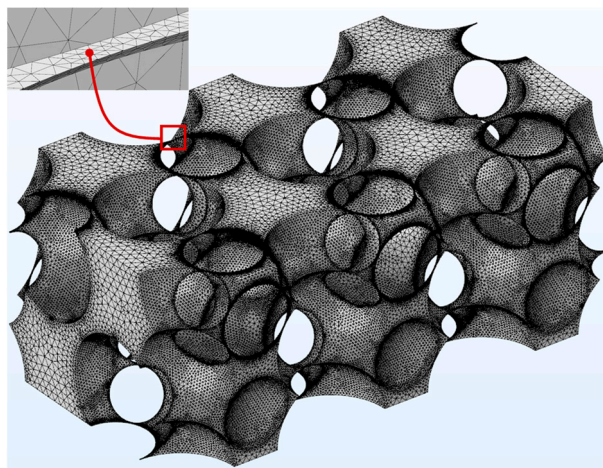
Figure 5. Example of the computational mesh developed for a certain inter-penetrating particle structure corresponding to $r_1 = 1.4$, $r_2 = 1$.

3. Results and Discussion

Figure 6 shows an example of the simulation results in terms of molar concentration profiles of species 1 (decane) for the case at $r_1 = 1.4$ and $r_2 = 1$ along the three chosen diffusional directions, which correspond to the x-, y-, and z-directions for the particular orientation chosen for the unit cell. The value of the concentration difference at the opposite faces is the same in the three cases (see Figure 4 and Table 2 for details).

Molar Concentration of w_1, mol m^{-3}
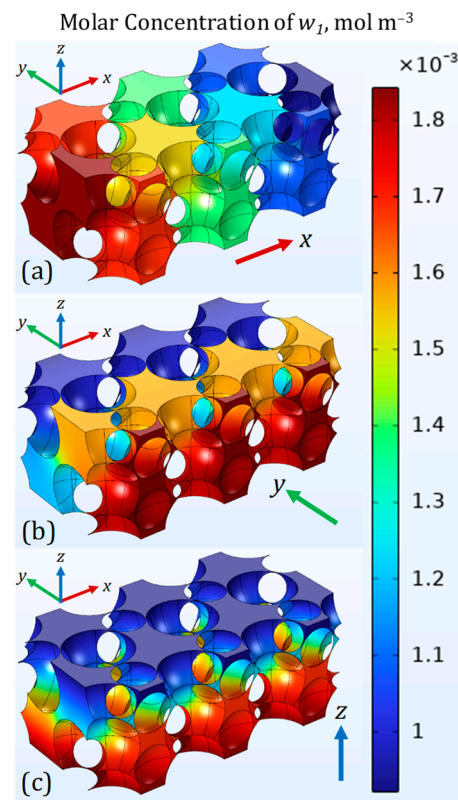
Figure 6. Concentration profiles of species 1 (decane), corresponding to the simulations along (**a**) x-direction, (**b**) y-direction, and (**c**) z-direction for $r_1 = 1.4$, $r_2 = 1$.

It can be observed that, for the particular choice of r_1 and r_2, this structure is made of inter-penetrating particles. For such types of structure, the steepest gradient is found near the inter-penetration boundaries (see also the previous Figure 5), which thus provided the highest deviation of the diffusional flux with respect to the virtual unconstrained straight lines. In fact, at a fixed concentration difference, when the streamlines are constrained to pass through narrow channels (small cross-sectional area), the related diffusional flux is higher, which implies a local higher concentration gradient according to Fick's law. Therefore, these regions are the main ones responsible for high tortuosity values, which theoretically reach the infinite value for completely disconnected regions [23].

Figure 7 shows the principal components of the tortuosity tensor (Equation (9)) along with the overall tortuosity (Equation (10)) as functions of r_1 for $r_2 = 1$. Let us recall that changing r_1 means changing the a/D_1 ratio, which in turn means that, for increasing r_1, the structure goes from a situation of particles' inter-penetration (higher tortuosity) to a larger unit cell, where particles are progressively farther from each other (lower tortuosity).

However, as the structure is anisotropic, the preferential paths of the diffusional flux could change direction due to the complex redistribution of the void space owing to the presence of new obstacles. Therefore, the change in the principal tortuosity components is not expected to be monotonic with the increasing/decreasing of r_1. This is just the situation depicted in the plots in Figure 7, where the components τ_{11} and τ_{33} show a maximum with r_1. As a consequence, the overall tortuosity shows a maximum as well.

Referring to the case at $r_1 = 1.5$, the highest tortuosity, τ_{11}, means that, along the direction identified by the first eigenvector, the diffusional flux is the lowest, which means that the path has more obstacles to diffusion. Additionally, the lowest tortuosity, τ_{33}, indicates the highest diffusional flux along the third eigenvector.

From a practical point of view, this means that the sample should be oriented along the third eigenvector to maximise the diffusion flux and along the first eigenvector to minimise it.
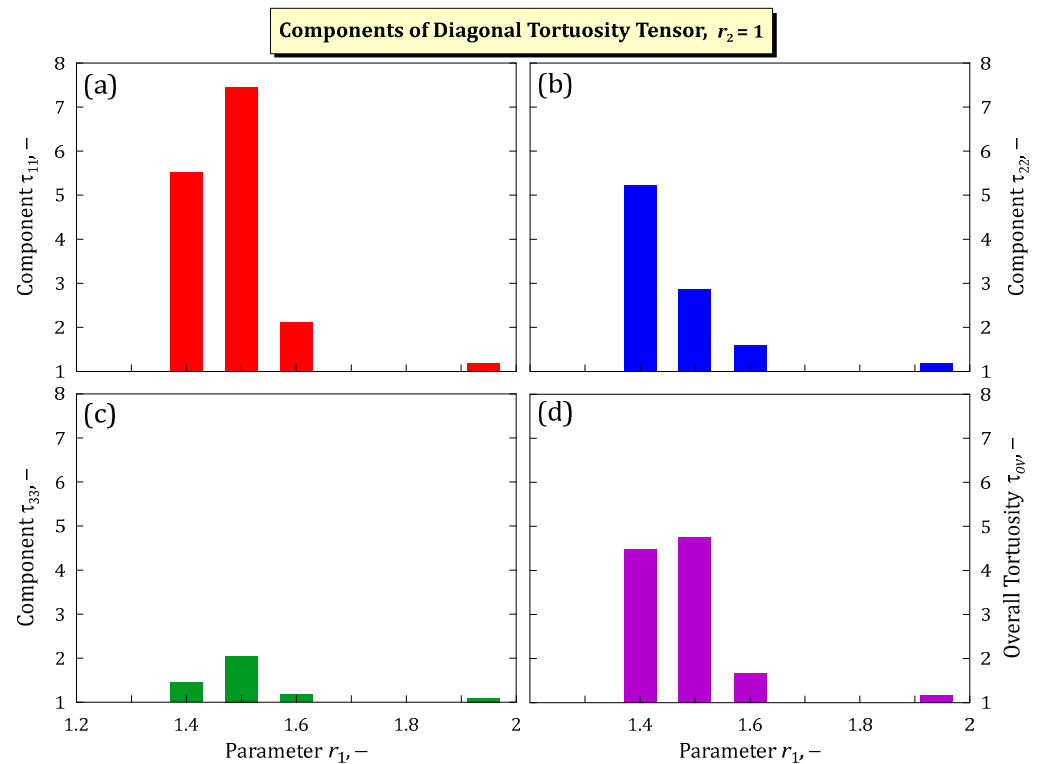
Figure 7. Principal components of the tortuosity tensor, τ_{ii}, (**a**–**c**), and overall tortuosity, τ_{ov} (**d**) as functions of r_1 for $r_2 = 1$.

This concept can be generally applied to the other structures, for which our study assesses important morphological properties that are not yet reported in the open literature.

Figure 8 shows the three eigenvectors for each of the structures considered in the present investigation. Specifically, the red vector corresponds to the highest effective diffusivity, the blue vector the middle one, and the green vector the lowest. Therefore, by looking at the length of the eigenvectors in each structure, one can directly observe the extent of the anisotropy: the more different the lengths, the higher the anisotropy level.

For a single structure, the lengths of the three vectors are proportional to their respective effective diffusivities and, thus, are comparable to each other. Differently, vectors of different structures cannot be compared with each other, as their lengths are adjusted to make them visible as a matter of clarity.

As can be observed, as the particle distance becomes larger (Figure 8a–d), which also means a larger structure, the geometry goes from inter-penetrating conditions to a non-inter-penetrating one, which also implies that the porosity gradually increases. In such an increasing procedure, all the components of the effective diffusivity tensor becomes progressively higher, which leads to progressively lower components of the tortuosity tensor.

As the lower bound for tortuosity is the unity, two consequences of a larger inter-particle distance are that the connectivity of the structure generally becomes gradually higher—even though some irregularity owing to the complexity of the geometry could be found at low porosity values—and that the structure becomes less anisotropic.

These geometrical and morphological considerations leads to the situation depicted in Figure 9, which shows the overall anisotropy factor and overall connectivity in the same conditions as those considered in Figure 7.
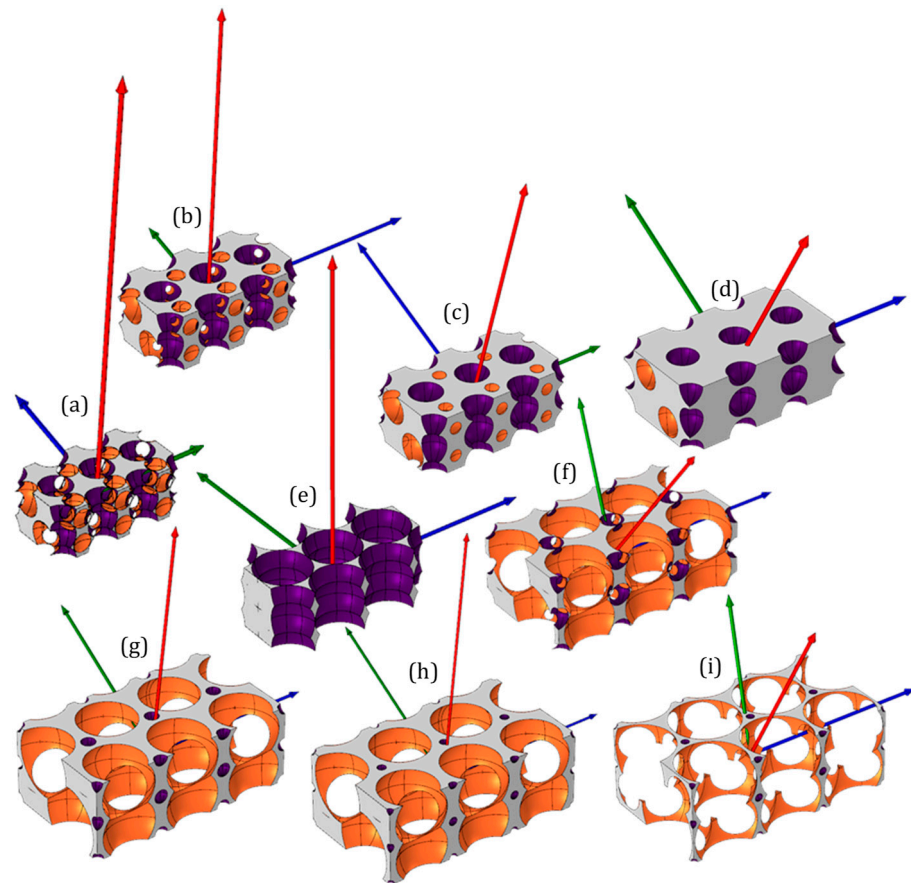
Figure 8. Principal diffusion directions (eigenvectors of the tortuosity tensor) for all the structures considered in the present work. The green, blue, and red colours represent the lowest, middle, and highest diffusional directions, respectively, corresponding to the lowest, middle, and highest eigenvalues. (**a**) $r_1 = 1.4$, $r_2 = 1$; (**b**) $r_1 = 1.5$, $r_2 = 1$; (**c**) $r_1 = 1.6$, $r_2 = 1$; (**d**) $r_1 = 1.94$, $r_2 = 1$; (**e**) $r_1 = 1$, $r_2 = 0.01$; (**f**) $r_1 = 3$, $r_2 = 3$; (**g**) $r_1 = 5$, $r_2 = 5$; (**h**) $r_1 = 8$, $r_2 = 8$; (**i**) $r_1 = 9$, $r_2 = 10$.
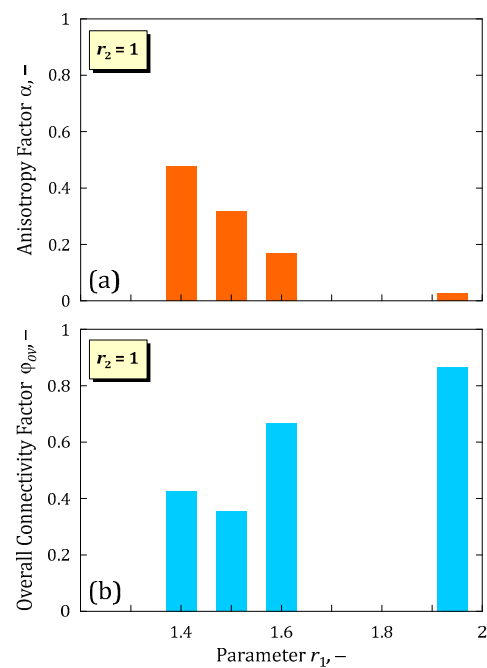
Figure 9. Anisotropy factor, α (**a**), and overall connectivity, φ_{ov} (**b**), as functions of r_1 for $r_2 = 1$.

Although these two parameters are calculated as average values (norm) of the three principal eigenvalues of the respective tensors (see Equations (10) and (11)), they provide useful information about the structures that is not so much related to their orientation but rather to their overall morphological properties.

Figure 10 shows the tortuosity tensor components and the overall tortuosity of all the structures considered in this work as functions of r_1 and r_2. Besides the particular values of the three components, it is possible to observe that, for all three components as well as the overall tortuosity, there are minima in the plot, which could be calculated more precisely by spanning the parameters r_1 and r_2 with a narrower grid of values.
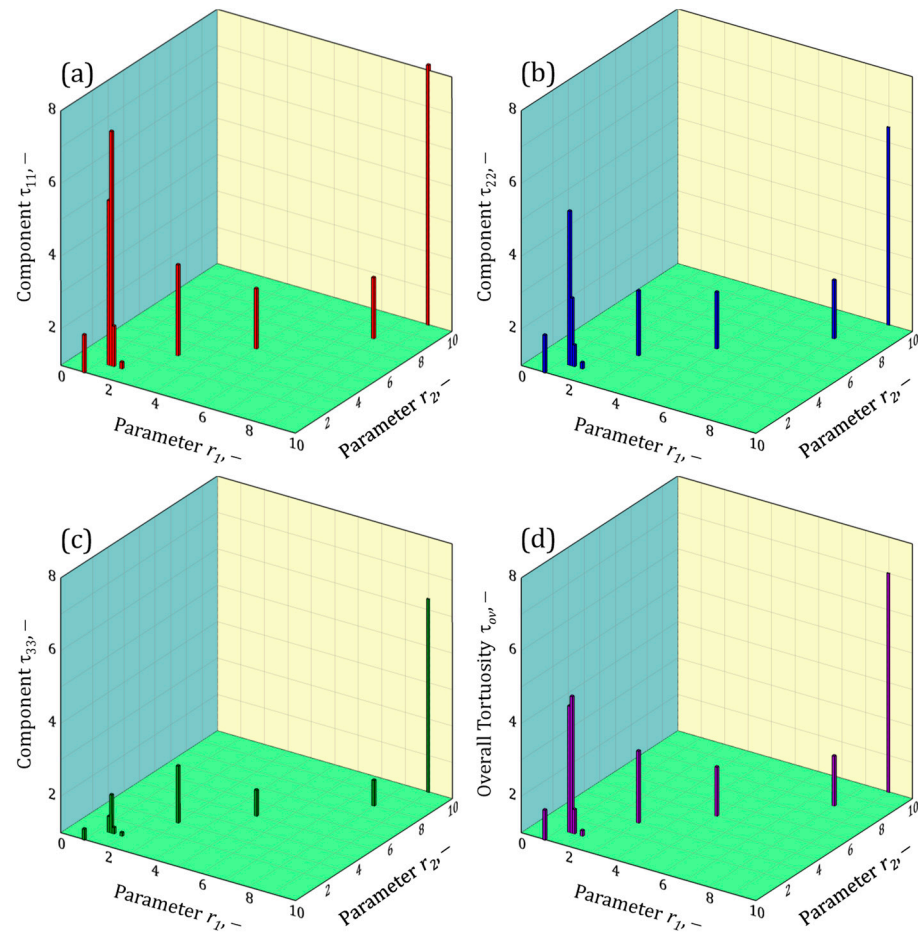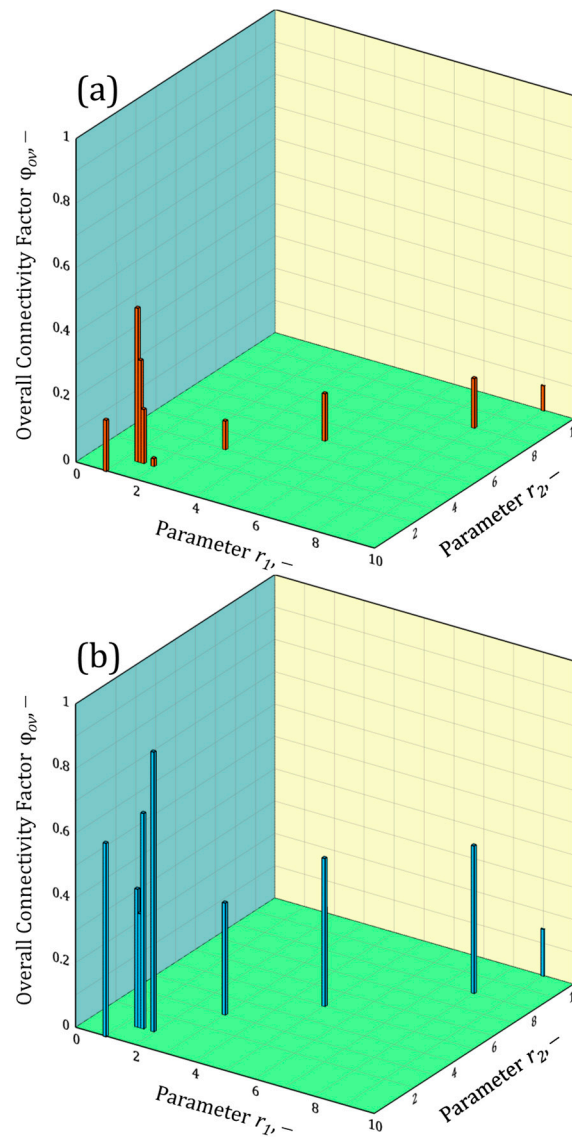

Figure 10. Principal components of the tortuosity tensor, τ_{ii} (**a**–**c**), and overall tortuosity, τ_{ov} (**d**), as functions of r_1 and r_2 for all the structures considered in the present work.

A low tortuosity is desirable, for example, to facilitate the mass transport through a porous structure, whereas a high value of it can be desirable for the intermediate layer for diffusion-barrier purposes.

What we want to underline here is that, to obtain a certain value of tortuosity, it is possible to work not only with the structure's spatial orientation, but also with the inter-particle geometrical distance, which can be obtained using a precise chemical synthesis and fabrication of the porous layer.

Figure 11 shows anisotropy and connectivity factors for the same values considered in Figure 10. It can be observed that the highest anisotropy is in the mathematical range of low values of r_1 and r_2, whereas lower anisotropy is found at higher values. This situation corresponds to the depiction in the previous Figure 8, where the eigenvectors' lengths, scaled according to the eigenvalues, are close to each other.

Figure 11. Anisotropy factor, α (**a**), and overall connectivity, φ_{ov} (**b**), as functions of r_1 and r_2 for all the structures considered in the present work.

4. Conclusions

In this work, a morphological investigation was carried out on MnTe-like structures via the evaluation of the tortuosity tensor as well as other morphological properties using a computational fluid dynamics (CFD) approach.

In particular, after choosing the two parameters determining the geometry of this bi-disperse structure (see above, the parameters r_1 and r_2) and constructing the necessary computational mesh, several CFD simulations were carried out using a novel three-dimensional methodology recently developed by our research group.

A total of nine structures were analysed in representation of the entire structure family, calculating the three principal components of the tortuosity tensor for each of them as well as anisotropy and connectivity factors, which quantitatively measured the dependence of morphology on the spatial orientation of the structure and the facility of the transport along the principal directions represented by the eigenvectors, respectively.

It was observed that high values of tortuosity components were found at both lower (=1 and 2) and higher (=9 and 10) values of $\{r_1, r_2\}$, which led to the conclusion that there must be at least a minimum at middle values. Additionally, the anisotropy factor was found to be higher at lower $\{r_1, r_2\}$ values and lower at higher $\{r_1, r_2\}$ values.

This was in line with the geometrical consideration that by increasing the inter-particle distance (represented a-dimensionally by r_1) and the ratio between particle diameters (represented a-dimensionally by r_2), the structure experienced an enlargement and a decreasing influence of one of the particles with respect to the other one, leading to a progressively more isotropic structure.

Overall, the morphological analysis in this paper provided new morphological information about the structure that can be exploited for existing practical purposes, as well as for future novel applications in new areas of science and technology. From this point of view, this work leads to wider future perspectives. In fact, some of the considered structures showed an interestingly high tortuosity if properly oriented, which means that layers with an effective diffusion barrier could be developed in the form of membranes or thin films. In this regard, the methodology used allowed us to preliminarily design the target material with the desired properties on a computer, thus saving time and resources. At the same time, the same procedure could be applied to other polymorphic forms in order to shed light on new and interesting morphological features that could be useful in tuning these materials for innovative applications.

Data Availability Statement: Simulation data will be made available upon reasonable request.

Conflicts of Interest: The authors declare that they have no conflicts of interest.

References

1. Kunitomi, N.; Hamaguchi, Y.; Anzai, S. Neutron diffraction study on manganese telluride. *Le J. Phys.* **1964**, *25*, 568–574. [CrossRef]
2. Allen, J.W.; Lucovsky, G.; Mikkelsen, J.C. Optical properties and electronic structure of crossroads material MnTe. *Solid State Commun.* **1977**, *24*, 367–370. [CrossRef]
3. Wei, S.H.; Zunger, A. Alloy-Stabilized Semiconducting and Magnetic Zinc-Blende Phase of MnTe. *Phys. Rev. Lett.* **1986**, *56*, 2391. [CrossRef] [PubMed]
4. Oleszkiewicz, J.; Kisiel, A.; Ignatowicz, S.A. Optical properties and dielectric function of manganese telluride thin films. *Thin Solid Films* **1988**, *157*, 1–6. [CrossRef]
5. Wang, C.; Kim, J.; Hughbanks, T. Synthesis and Structure of Novel Ternary Manganese Tellurides: $MMnTe_2$ (M = Li, Na), $Na_3Mn_4Te_6$, and $Na_3Mn_{4.7}Te_6$. *MRS Online Proc. Libr.* **1996**, *453*, 23. [CrossRef]
6. Kriegner, D.; Výborný, K.; Olejník, K.; Reichlová, H.; Novák, V.; Marti, X.; Gazquez, J.; Saidl, V.; Němec, P.; Volobuev, V.V.; et al. Multiple-stable anisotropic magnetoresistance memory in antiferromagnetic MnTe. *Nat. Commun.* **2016**, *7*, 11623. [CrossRef]
7. Han, Y.; Holder, A.M.; Siol, S.; Lany, S.; Zhang, Q.; Zakutayev, A. Zinc-Stabilized Manganese Telluride with Wurtzite Crystal Structure. *J. Phys. Chem. C* **2018**, *122*, 18769–18775. [CrossRef]
8. Luo, Y.; Wang, J.; Yang, J.; Mao, D.; Cui, J.; Jia, B.; Liu, X.; Nielsch, K.; Xu, X.; He, J. Microstructural iterative reconstruction toward excellent thermoelectric performance in MnTe. *Energy Environ. Sci.* **2023**, *16*, 3743–3752. [CrossRef]
9. Li, X.; Yang, B.; Li, S.; Xie, H.; Wang, X.; Zhong, H.; Shen, H.; Tang, J. First-principles calculations to investigate probing the influence of Mn and Mg doping concentration on electronic structures and transport properties of SnTe alloys. *Results Phys.* **2023**, *48*, 106443. [CrossRef]
10. Shah, S.I.A.; Saleem, A.; Munawar, S.; Khan, K.Z.; Osman, S.M.; Ehsan, M.F.; Manzoor, S. Facile fabrication of manganese telluride and graphene oxide nanostructure for robust energy storage systems. *J. Korean Ceram. Soc.* **2024**, *61*, 605–613. [CrossRef]

11. Selestina, A.; Vijay, V.; Karunagaran, N.; Navaneethan, M. Thermoelectric performance of lead-free manganese telluride via alkaline Mg doping for mid-temperature application. *J. Alloys Compd.* **2024**, *976*, 17284. [CrossRef]

12. Autieri, C. New type of magnetism splits from convention. *Nature* **2024**, *626*, 482–483. [CrossRef] [PubMed]

13. Lee, S.; Lee, S.; Jung, S.; Jung, J.; Kim, D.; Lee, Y.; Seok, B.; Kim, J.; Park, B.G.; Šmejkal, L.; et al. Broken Kramers Degeneracy in Altermagnetic MnTe. *Phys. Rev. Lett.* **2024**, *132*, 036702. [CrossRef] [PubMed]

14. Chowde Gowda, C.; Chandravanshi, D.; Tromer, R.M.; Malya, A.; Chattopadhyay, K.; Galvão, D.S.; Tiwary, C.S. Tuning the band gap of manganese telluride quantum dots (MnTe QDs) for photocatalysis. *Appl. Phys. A* **2024**, *130*, 299. [CrossRef]

15. Zhao, C.; Caravella, A.; Xu, H.; Brunetti, A.; Barbieri, G.; Goldbach, A. Support mass transfer resistance of Pd/ceramic composite membranes in the presence of sweep gas. *J. Membr. Sci.* **2018**, *550*, 365–376. [CrossRef]

16. Peters, T.; Caravella, A. Pd-based Membranes: Overview and Perspectives. *Membranes* **2019**, *9*, 25. [CrossRef]

17. Liu, J.; Bellini, S.; Sun, Y.; Pacheco Tanaka, D.A.; Tang, C.; Li, H.; Gallucci, F.; Caravella, A. Hydrogen Permeation and Stability in Ultra-thin Pd-Ru Supported Membranes. *Int. J. Hydrogen Energy* **2020**, *45*, 7455–7467. [CrossRef]

18. Caravella, A.; Prenesti, G.; Martinez-Diaz, D.; Alique, D.; Hara, S. Optimal Permeance Ratio, Flux Direction and Layer Distribution in Composite Asymmetric Membranes composed of Sequences of Layers obeying Real-Power Flux Laws. *J. Membr. Sci.* **2024**, *705*, 122877. [CrossRef]

19. Caravella, A.; Fiore, P.; Azzato, G.; De Marco, G. Novel connectivity tensor for a systematic assessment of topology and anisotropy of real membranes and microporous structures. *Chem. Eng. Sci.* **2023**, *268*, 118386. [CrossRef]

20. Krause, M.; Bechstedt, F. Structural and magnetic properties of MnTe phases from *ab initio* calculations. *J. Supercond. Nov. Magn.* **2013**, *26*, 1963–1972. [CrossRef]

21. Kim, A.S.; Chen, H. Diffusive tortuosity factor of solid and soft cake layers: A random walk simulation approach. *J. Membr. Sci.* **2006**, *279*, 129–139. [CrossRef]

22. Basser, J.P.; Pierpaoli, C. Microstructural and Physiological Features of Tissues Elucidated by Quantitative-Diffusion-Tensor MRI. *J. Magn. Reson. Ser. B* **1996**, *111*, 209–219. [CrossRef] [PubMed]

23. Azzato, G.; De Marco, G.; Stellato, V.; Sun, Y.; Caravella, A. Tortuosity and Connectivity Evaluation by CFD Simulation for Morphological Characterization of Membranes and Catalytic Structures. Case Study: CaF_2-like Structure. *Chem. Eng. Sci.* **2019**, *195*, 519–530. [CrossRef]

24. Bellini, S.; Azzato, G.; Grandinetti, M.; Stellato, V.; De Marco, G.; Sun, Y.; Caravella, A. A Novel Connectivity Factor for Morphological Characterization of Membranes and Porous Media: A Simulation Study on Structures of Mono-sized Spherical Particles. *Appl. Sci.* **2018**, *8*, 573. [CrossRef]

25. Whitaker, S. Simultaneous heat, mass and momentum transfer in porous media: A theory of drying. *Adv. Heat Transf.* **1977**, *13*, 119–203. [CrossRef]

26. Kim, J.H.; Ochoa, J.A.; Whitaker, S. Diffusion in Anisotropic Porous Media. *Transp. Porous Media* **1987**, *2*, 327–356. [CrossRef]

27. Alam, P.; Byholm, T.; Toivakka, M. Calculating tortuosity in quasi-random anisotropic packings. *Nord. Pulp Pap. Res. J.* **2006**, *21*, 670–675. [CrossRef]

28. Matyka, M.; Khalili, A.; Koza, Z. Tortuosity-porosity relation in porous media flow. *Phys. Rev. E—Stat. Nonlinear Soft Matter Phys.* **2008**, *78*, 026306. [CrossRef] [PubMed]

29. Vallavh, R. Modeling Tortuosity in Fibrous Porous Media Using Computational Fluid Dynamics. Ph.D. Thesis, North Carolina State University, Raleigh, NC, USA, 2009.

30. Rezanezhad, F.; Quinton, W.L.; Price, J.S.; Elrick, D.; Elliot, T.R.; Heck, R.J. Examining the effect of pore size distribution and shape on flow through unsaturated peat using 3-D computed tomography. *Hydrol. Earth Syst. Sci. Discuss.* **2009**, *6*, 3835. [CrossRef]

31. Yamashita, T.; Suzuki, K.; Adachi, H.; Nishino, S.; Tomota, Y. Effect of microscopic internal structure on sound absorption properties of polyurethane foam by x-ray computed tomography observations. *Mater. Trans.* **2009**, *50*, 373–380. [CrossRef]

32. Szczepanski, Z.; Cieszko, M.; Zych, G. Application of Micro Computer Tomography to Identification of Pore Structure Parameters of Porous Materials. *Nanotechnol. Mater.* **2010**, *1*, 90–91. Available online: https://yadda.icm.edu.pl/baztech/element/bwmeta1.element.baztech-2c662df5-bba1-4597-a749-beef641857d4/c/Szczepanski.pdf (accessed on 28 August 2024).

33. Duda, A.; Koza, Z.; Matyka, M. Hydraulic tortuosity in arbitrary porous media flow. *Phys. Rev. E—Stat. Nonlinear Soft Matter Phys.* **2011**, *84*, 036319. [CrossRef] [PubMed]

34. Sobieski, W.; Zhang, Q.; Liu, C. Predicting tortuosity for airflow through porous beds consisting of randomly packed spherical particles. *Transp. Porous Media* **2012**, *93*, 431–451. [CrossRef]

35. Wang, P. Lattice Boltzmann simulation of permeability and tortuosity for flow through dense porous media. *Math. Probl. Eng.* **2014**, *2014*, 694350. [CrossRef]

36. Berg, C.F. Permeability description by characteristic length, tortuosity, constriction and porosity. *Transp. Porous Media* **2014**, *103*, 381–400. [CrossRef]

37. Herremans, E.; Verboven, P.; Verlinden, B.E.; Cantre, D.; Abera, M.; Wevers, M.; Nicolai, B.M. Automatic analysis of the 3-D microstructure of fruit parenchyma tissue using X-ray micro-CT explains differences in aeration. *BMC Plant Biol.* **2015**, *15*, 264. [CrossRef]